

# PoGaIN: Poisson-Gaussian Image Noise Modeling from Paired Samples

Nicolas Bähler\*, Majed El Helou\*, Étienne Objois, Kaan Okumuş, and Sabine Süsstrunk, *Fellow, IEEE*.

**Abstract**—Image noise can often be accurately fitted to a Poisson-Gaussian distribution. However, estimating the distribution parameters from only a noisy image is a challenging task. Here, we study the case when paired noisy and noise-free samples are available. No method is currently available to exploit the noise-free information, which holds the promise of achieving more accurate estimates. To fill this gap, we derive a novel, cumulant-based, approach for Poisson-Gaussian noise modeling from paired image samples. We show its improved performance over different baselines with special emphasis on MSE, effect of outliers, image dependence and bias, and additionally derive the log-likelihood function for further insight and discuss real-world applicability.

**Index Terms**—Image Noise, Noise Estimation, Poisson-Gaussian Noise Modeling, Paired Samples Modeling

## I. INTRODUCTION

Noise always affects captured images in any imaging pipeline. It is commonly categorized into a shot noise component and a read noise component. The former noise component is commonly modeled with a Poisson distribution, emerging from the particle nature of light whose intensity the sensor estimates over a finite duration of time. The latter is generally modeled with a Gaussian distribution, notably for raw images that are not yet passed through the image processing pipeline, which can modify the distribution. Modeling noise distribution is thus crucial for analyzing imaging devices and datasets [1], [2], and developing denoising methods, notably noise-aware ones [3], [4].

In their seminal work, Foi *et al.* [5] propose a Poisson-Gaussian model for the noise distribution. The authors also propose a clever solution for fitting the noise model parameters from a noisy input image. Their algorithm begins with local expectation and standard deviation estimates from image parts that are assumed to depict a single underlying intensity value. The global parametric model is then fitted through a maximum likelihood search based on the local estimates. Multiple assumptions are made in order to reach a final estimate, in part due to the lack of input information beyond the noisy image. However, when modeling datasets or analyzing an imaging system, we may be able to acquire paired noisy and noise-free images. In this paper, we exploit this additional information

and study the problem of modeling the noise *with paired samples*.

We propose a novel method that estimates the parameters of the aforementioned noise model based on noisy and noise-free image pairs. The additional information of the noise-free version of a given image enables our approach to outperform the method introduced by Foi *et al.* [5] significantly. We additionally train a neural network based noise model estimator and show that we also outperform this learning-based alternative. Finally, we introduce a variance-based baseline method, which also takes advantage of noisy and noise-free image pairs to be able to compare.

## II. RELATED WORK

Denoising is one of the most fundamental tasks in image restoration. It has significant importance, both from an application point of view, and theoretically. Most classic denoisers, for instance PURE-LET [6], KSVD [7], WNNM [8], BM3D [9], and EPLL [10], require knowledge of the noise level in the input test image. Deep learning image denoisers that have shown improved empirical performance [11], [12] also require knowledge of noise distributions, if not at test time [13], then at least for training [3], [14]. This is due to the degradation overfitting of deep neural networks [15]. Noise modeling is thus important for both denoisers at test time, and also for acquisition system analysis and dataset modeling for training these denoisers. Research has focused on modeling noise from noisy images without relying on ground truth, i.e., noise-free, information [5]. However, when ground truth information is available it cannot readily be exploited to improve the modeling, for example in the practical Poisson-Gaussian noise settings [1], [2]. Both FMD [1] and W2S [2] thus rely on a noise modeling method that does not consider ground truth noise-free images [5]. To our best-knowledge, no method exploiting the additional noise-free information is available. Hence, we propose such a solution for modeling the Poisson-Gaussian image noise distribution (PoGaIN), which exploits paired samples (noisy and noise-free images) to significantly improve the modeling accuracy. Our approach is based on the cumulant expansion, which is also used by other authors to derive estimators for PoGaIN model parameters, but for different settings like noisy image time series [16] or single noisy images [17].

## III. MATHEMATICAL FORMULATION

### A. Poisson-Gaussian model

The Poisson-Gaussian noise model outlined by Foi *et al.* [5] consists of two components, the Poisson shot noise and

\* Both authors have equal contributions.

Submitted for review on October 10th, 2022.

Work carried out in the Image and Visual Representation Lab (IVRL) at the School of Computer and Communication Sciences, EPFL, Switzerland. [>{nicolas.bahler, sabine.susstrunk}@epfl.ch](mailto:{nicolas.bahler, sabine.susstrunk}@epfl.ch), [>melhelou@ethz.ch](mailto:melhelou@ethz.ch).

Corresponding author: Nicolas Bähler

All code and supplementary material at <https://github.com/IVRL/PoGaIN>

the Gaussian read noise, which are assumed to be independent. The signal-dependent Poisson component  $\eta_p$  and signal-independent Gaussian component  $\eta_g$  are defined, respectively, by

$$\eta_p = \frac{1}{a}\alpha, \quad \eta_g = \beta, \quad \alpha \sim \mathcal{P}(ax), \quad \beta \sim \mathcal{N}(0, b^2), \quad (1)$$

where  $x$  is the ground truth (noise-free) signal, and  $a$  and  $b$  are distribution parameters. The complete model is made up of the sum of these two components

$$y = \eta_p + \eta_g = \frac{1}{a}\alpha + \beta, \quad (2)$$

where  $y$  is the observed (noisy) signal. We note to the reader that the  $a$  and  $b$  in [5] correspond to our  $\frac{1}{a}$  and our  $b^2$ , respectively. Thus,  $a$  is equal to percent quantum efficiency.

As derived in the supplementary material, the following properties hold for  $\eta_p$

$$\mathbb{E}[\eta_p] = x, \quad \mathbb{V}[\eta_p] = \frac{x}{a}, \quad (3)$$

which shows that the Poisson component is indeed signal-dependent and that the Gaussian component, having constant mean and variance, is signal independent. Consequently, we derive the expected value and variance of the observation  $y$

$$\mathbb{E}[y] = x, \quad \mathbb{V}[y] = \frac{x}{a} + b^2. \quad (4)$$

### B. Likelihood derivation

The noise model, presented in Equation (2), leads to the following expression for the likelihood

$$\mathcal{L}(y|a, b, x) = \prod_i \sum_{k=0}^{\infty} \frac{(ax_i)^k}{k!b\sqrt{2\pi}} \exp\left(-ax_i - \frac{(y_i - k/a)^2}{2b^2}\right), \quad (5)$$

where  $y$  is the captured noisy image,  $x$  is the ground truth noise-free image and  $i$  is the pixel index in the vectorized representation of an image. The complete derivation of the likelihood function is given in the supplementary material. The noise parameters  $\hat{a}$  and  $\hat{b}$  that optimize for the maximum likelihood are then given by

$$\hat{a}, \hat{b} = \arg \max_{a, b} \mathcal{L}(y|a, b, x). \quad (6)$$

Optimizing over the log-likelihood  $\mathcal{L}\mathcal{L}$  is computationally inefficient. To improve convergence, we truncate the summation over  $k$  to a  $k_{max}$  such as most of the weight of the sum lies in  $k$  values below  $k_{max}$  (details in code). Nonetheless, optimizing  $\mathcal{L}\mathcal{L}$  is no viable solution to our problem. But the log-likelihood can still provide empirical insight, as we show in our Analysis V-D2.

## IV. PROPOSED METHOD

Rather than interpreting  $x$  and  $y$  as two observed images, we consider  $x$  and  $y$  as a collection of samples from two distributions  $\mathcal{X}$  and  $\mathcal{Y}$  and define a random variable  $X \sim \mathcal{X}$  such that

$$\mathbb{P}[X = x_i] = \frac{|\{k : x_k = x_i\}|}{n}, \quad (7)$$

where  $n$  corresponds to the number of samples (i.e., the number of pixels in  $x$  and  $y$ ). We define  $\mathcal{Y}$  to be the distribution of the Poisson-Gaussian noise model over the distribution  $\mathcal{X}$ . Formally, introducing another random variable  $Y \sim \mathcal{Y}$ , we get

$$Y \sim \mathcal{Y} = \frac{\mathcal{P}(a\mathcal{X})}{a} + \mathcal{N}(0, b^2). \quad (8)$$

Next, we can obtain the 2-nd and 3-nd cumulant of  $\mathcal{Y}$  as a system of equations

$$\begin{cases} \kappa_2[\mathcal{Y}] = \frac{\bar{x}}{a} + \bar{x}^2 - \bar{x}^2 + b^2 \\ \kappa_3[\mathcal{Y}] = \bar{x}^3 - 3\bar{x}^2\bar{x} + 2\bar{x}^3 + 3\frac{\bar{x}^2}{a} - 3\frac{\bar{x}^2}{a} + \frac{\bar{x}}{a^2} \end{cases}, \quad (9)$$

where  $\bar{x}$  denotes the mean of  $x$  (for example  $\bar{x}^{k,j} = (\frac{1}{n} \sum_i x_i^k)^j$ ). Both  $\kappa_2[\mathcal{Y}]$  and  $\kappa_3[\mathcal{Y}]$  can be estimated with an unbiased estimator (k-statistic). Therefore, Equations (9) form a system of two equations, with two unknowns  $a$  and  $b$ , which is solved by our cumulant-based method (**OURS**).

## V. EXPERIMENTAL EVALUATION

### A. Data processing

The dataset we use is based on the Berkeley Segmentation Dataset 300 [18]. We synthesize noise stochastically by picking a seed  $s \in \{0, \dots, 9\}$ ,  $a \in [1, 100]$  and  $b \in [0.01, 0.15]$  resulting in noisy and noise-free image pairs. For validation, we pick 10 images out of the test set of the Berkeley Segmentation Dataset 300 [18]. For each seed  $s \in \{0, \dots, 9\}$ , and for 25 linearly spaced values for  $a \in [1, 100]$  and  $b \in [0.01, 0.15]$ , we synthesize an image pair, resulting in a total of 62500 pairs for evaluation.

### B. Baseline methods

1) *FOI*: As we briefly mention above, the method proposed by Foi *et al.* [5] estimates  $a$  and  $b$  by segmenting pixels assumed to have the same underlying value but simply being distorted by noise into non-overlapping intensity level sets. Further, a local estimation of multiple expectation and standard-deviation pairs is carried out before, finally, a global parametric model fitting those local estimates is performed. *FOI* only uses  $y$ , and does not provide a way to exploit  $x$  when it is available. This makes a good estimation of  $a$  and  $b$  more challenging.

2) *CNN*: For the sake of extended comparison, we design a convolutional neural network (CNN) that we train to predict  $a$  and  $b$ . The detailed architecture of the CNN can be found described in our code repository. The CNN takes only the noisy image  $y$  as input. We cannot rule out that a more complex neural network based solution could outperform this CNN. We provide it as an additional baseline, and it is not the focus of this paper.

3) *VAR*: For fairness of comparison, we design a baseline method that also takes advantage of noisy and noise-free image pairs. To derive it, we define  $Y_i = \{y_j : x_j = x_i\}$  as the set of all pixels of  $y$  for which the corresponding pixel in  $x$  has the same intensity as  $x_i$ . This approach is based on the variance

across the pixel sets  $Y_i$ . First, the theoretical mean of  $Y_i$  is  $x_i$ , and hence we can compute the empirical variance of  $Y_i$

$$\mathbb{V}[Y_i] = \frac{1}{|Y_i|} \sum_{y_k \in Y_i} (y_k - x_i)^2. \quad (10)$$

We additionally have that  $y_j \sim \frac{\mathcal{P}(ax_i)}{a} + \mathcal{N}(0, b^2)$ . Thus, according to Equation (4),  $\mathbb{V}[Y_i] \approx \frac{x_i}{a} + b^2$ . Using this observation, we select  $a, b$  such that the above approximation holds as closely as possible between the two values for any given  $i$ , where  $\mathbb{V}[Y_i]$  is computed using Equation (10). Finally, we obtain an estimation of  $a, b$  by computing

$$\hat{a}, \hat{b} = \arg \min_{a, b} \sum_i \left( \mathbb{V}[Y_i] - \frac{x_i}{a} - b^2 \right)^2. \quad (11)$$

In our experiments, images have 8-bit depth, and thus we only have 256 possible values for  $x_i$ . Hence, we can expect that sufficiently many pixels share the same intensity. But this assumption is a limitation of this method, because it relies on images having few different pixel intensities (sparse histogram) and having a large dynamic range to get robust empirical variance values  $\mathbb{V}[Y_i]$ . Further, note that in Equation (11), the same intensity level  $x_i$  is appearing in the sum  $|Y_i|$  times, and thus introduces bias.

### C. Experimental results

First, we provide results statistics of the Mean Squared Error (MSE) for the estimates  $\hat{a}^{-1}, \hat{b}^2$  of the different methods compared to the ground truth values  $a^{-1}, b^2$  in Tables I and II.

TABLE I  
STATISTICS ABOUT THE MSE ERROR ON  $\hat{a}^{-1}$  FOR VARIOUS METHODS.

Method	Mean	Standard Dev.	75%-Quantile	Maximum
<i>FOI</i>	$3.15 \times 10^3$	$7.46 \times 10^5$	$5.64 \times 10^{-4}$	$1.86 \times 10^8$
<i>CNN</i>	$1.78 \times 10^{-2}$	$8.67 \times 10^{-2}$	$7.40 \times 10^{-5}$	$6.34 \times 10^{-1}$
<i>VAR</i>	$8 \times 10^{-6}$	$8.50 \times 10^{-5}$	$\approx 0$	$3.54 \times 10^{-3}$
<b><i>OURS</i></b>	$3 \times 10^{-6}$	$1.40 \times 10^{-5}$	$1 \times 10^{-6}$	$2.77 \times 10^{-4}$

TABLE II  
STATISTICS ABOUT THE MSE ERROR ON  $\hat{b}^2$  FOR VARIOUS METHODS.

Method	Mean	Standard Dev.	75%-Quantile	Maximum
<i>FOI</i>	$3.46 \times 10^{-1}$	6.67	$9.40 \times 10^{-5}$	$6.16 \times 10^2$
<i>CNN</i>	$8 \times 10^{-6}$	$2.30 \times 10^{-5}$	$5 \times 10^{-6}$	$3.87 \times 10^{-4}$
<i>VAR</i>	$1 \times 10^{-6}$	$1.10 \times 10^{-5}$	$\approx 0$	$4.45 \times 10^{-4}$
<b><i>OURS</i></b>	$\approx 0$	$1 \times 10^{-6}$	$\approx 0$	$3.30 \times 10^{-5}$

*FOI* performs the worst compared to the other methods in our experimental setting. This performance is expected to a certain extent, because the method only uses  $y$ , as is *CNN* (which performs better). Thus, for most of the following graphs and plots, we only focus on our method ***OURS*** compared with the baseline methods *CNN* and *VAR*.

1) *Mean squared error*: The MSE of  $\hat{a}^{-1}$  is dependent on the value of  $a$ . We can see in Figure 1 that the smaller  $a$ , the bigger the error on  $\hat{a}^{-1}$ . This is a consequence of using  $\frac{1}{a}$  in our noise model. When  $a$  is small, the Poisson noise is dominant and when  $a$  increases its contribution to the noise

model gradually vanishes. Even though the MSE on  $\hat{b}^2$  does not depend significantly on the value of  $b$ , as it is roughly constant for all methods except the *CNN*, instances with less overall noise (large  $a$  and small  $b$ ) lead to smaller MSE values.

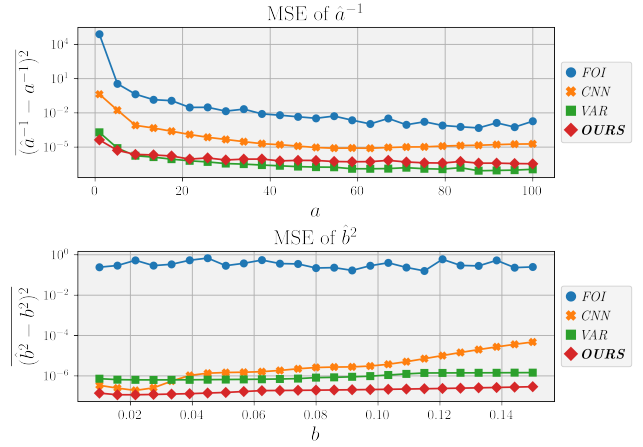


Fig. 1. MSE for each method as a function of  $a$  (top) and  $b$  (bottom). Note that the error axis is in log scale.

We note that our method consistently outperforms *CNN*. Additionally, we also see that ***OURS*** achieves a roughly 10 times smaller MSE value on  $\hat{b}^2$  than *VAR*, while *VAR* slightly improves MSE on  $\hat{a}^{-1}$ , and particularly for larger  $a$ .

2) *Effect of outliers and image dependence*: We analyze the effect that outliers have on the overall performance. We consider samples as outliers when  $\text{MSE} > Q(0.75) + 1.5 * (Q(0.75) - Q(0.25))$  where  $Q(0.25)$  and  $Q(0.75)$  are the first and the third quartiles, respectively. We remove those outlier values, and Table III shows the percentage of data remaining after filtering. We show performance with and without outliers in Fig 2. Excluding outliers improves the performance significantly.

TABLE III  
PERCENTAGE OF DATA NOT ELIMINATED AS OUTLIERS.

Method	$a$ -based outliers	$b$ -based outliers	Combined
<i>CNN</i>	82.17 %	84.14 %	70.18 %
<i>VAR</i>	85.16 %	85.74 %	81.93 %
<b><i>OURS</i></b>	<b>87.81 %</b>	<b>88.95 %</b>	<b>82.83 %</b>

Further, the MSE varies depending on the intrinsic properties of the noise-free images  $x$ . We illustrate the dependence of the MSE on 10 different ground truth images used for validation in Figure 2. We average over all different seeds and over the  $a$  or  $b$  values, respectively. We observe that the ground truth image influences the estimation performance for the  $b$  parameter more significantly. Additionally, we note that ***OURS*** is the most robust when it comes to causing outlier error values, whereas *CNN* is most prone to producing outliers.

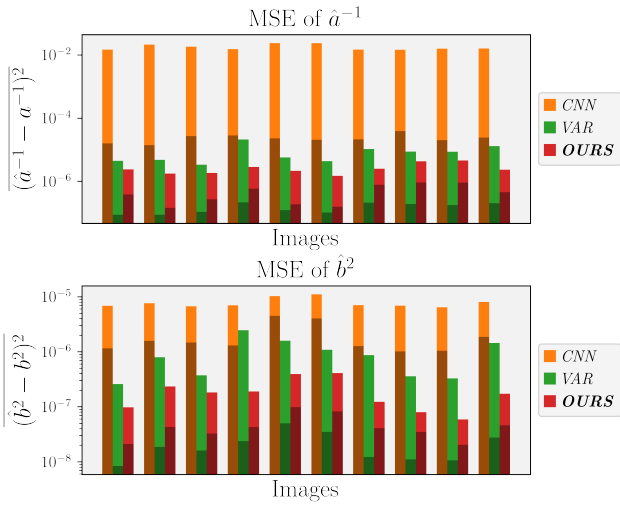


Fig. 2. MSE dependence on 10 images for  $\hat{a}^{-1}$  (top) and  $\hat{b}^2$  (bottom), including outliers (bright colors) and excluding outliers (dark colors). Note that the error axis is in log scale.

#### D. Analysis

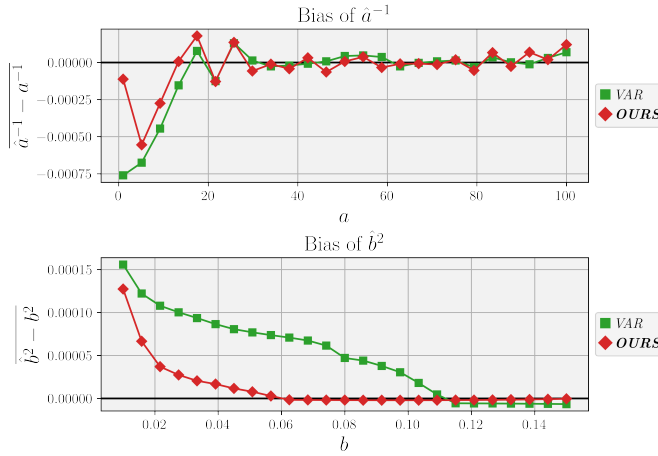


Fig. 3. Absolute estimation error, illustrating the bias in  $\hat{a}^{-1}$  (top) and  $\hat{b}^2$  (bottom) of estimators **VAR** and **OURS**, for varying  $a, b$  values. Note that the bias axis is in linear scale.

1) *Bias*: Figure 3 shows that the bias is most significant for both the smallest values of  $a$  and of  $b$ , although that the bias is small in general. For **OURS** and  $\hat{a}^{-1}$ , this bias is explained by the variance of  $\kappa_3[\mathcal{Y}]$  from Equation (9), as this variance is dependent on  $\frac{1}{a}$  and is larger when  $a$  is small. Further, the bias on  $\hat{b}^2$  is explained by the fact that we only keep *real* values of  $\hat{b}$ , discarding negative estimates of  $\hat{b}^2$ . By eliminating negative estimates, we introduce a positive bias. For **VAR**, Equation (11) shows that under-estimating  $\hat{b}$  leads to an over-estimation of  $\frac{1}{\hat{a}}$ , which highlights the challenging un-mixing of the two noise parameters in this setup. Figure 3 also shows that **VAR** is always biased in  $b$  while for **OURS** the bias becomes zero for  $b > 0.06$ .

2) *Log-likelihood*: As discussed in section V-D2,  $\mathcal{LL}$  cannot be optimized for global minima efficiently. However, empirically,  $\mathcal{LL}$  can give additional insight. In Figure 4, we show the relative absolute difference between  $\mathcal{LL}$

for the actual values  $a, b$  and their estimates  $\hat{a}, \hat{b}$  averaged over the validation images and seeds for different methods;

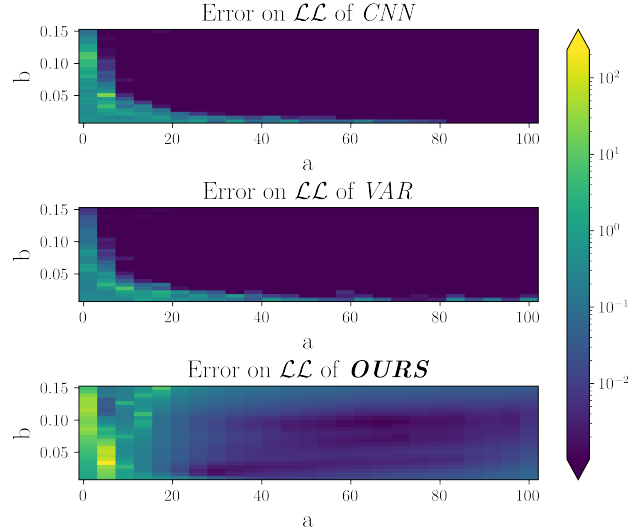
$$\left| \frac{\mathcal{LL}(y|\hat{a}, \hat{b}, x) - \mathcal{LL}(y|a, b, x)}{\mathcal{LL}(y|a, b, x)} \right|.$$


Fig. 4. Relative absolute difference between the  $\mathcal{LL}$  computed for the estimated parameters, and the actual  $\mathcal{LL}$  of the ground truth parameters. Note that the error axis is in log scale.

According to Figure 4, on average, **VAR** and **CNN** result in estimates that are more likely, but, as shown earlier, perform worse than **OURS** in general. This is due to the complexity of the statistical distribution of the noise model leading to a mismatch between likelihood-maximization and expected-error-minimization estimators.

3) *Real-world scenario*: For real-world applications, the Poisson component often dominates the noise model ( $a$  is small). **OURS** achieves smaller MSE than **VAR** when  $a$  is small. Therefore, while **VAR** can provide more accurate  $a$  estimates in certain cases, in real-world applications **OURS** outperforms the baseline. Further, **OURS** is more robust to outlier errors, is less biased and consistently achieves smaller MSE on  $\hat{b}^2$ . Additionally, **VAR** relies on images having a sparse histogram and large dynamic range. For all those additional reasons, **OURS** is better suited for real-world applications, too.

## VI. CONCLUSION

We propose an efficient cumulant-based Poisson-Gaussian noise estimator for paired noisy and noise-free images. Our method significantly outperforms prior baselines, notably a neural network solution and a variance-based method, both of which we design. Finally, the log-likelihood that we derive enables us to demonstrate the intrinsic difficulty of the problem our method tackles.

In future work, one could explore fine-tuning the weights of the **VAR** baseline and taking into account the clipping behavior of digital sensors in real-world applications. Furthermore, we note that our method can be used as a starting point to speed up the optimization for maximizing the likelihood function that we derive, if likelihood —rather than inverse expected error—is to be maximized.

## REFERENCES

- [1] Y. Zhang, Y. Zhu, E. Nichols, Q. Wang, S. Zhang, C. Smith, and S. Howard, "A Poisson-Gaussian denoising dataset with real fluorescence microscopy images," in *Proceedings of the IEEE/CVF Conference on Computer Vision and Pattern Recognition*, 2019, pp. 11 710–11 718.
- [2] R. Zhou, M. El Helou, D. Sage, T. Laroche, A. Seitz, and S. Süsstrunk, "W2S: microscopy data with joint denoising and super-resolution for widefield to SIM mapping," in *European Conference on Computer Vision Workshops*, 2020, pp. 474–491.
- [3] M. El Helou and S. Süsstrunk, "Blind universal Bayesian image denoising with Gaussian noise level learning," *IEEE Transactions on Image Processing*, vol. 29, pp. 4885–4897, 2020.
- [4] L. D. Tran, S. M. Nguyen, and M. Arai, "GAN-based noise model for denoising real images," in *Proceedings of the Asian Conference on Computer Vision*, 2020.
- [5] A. Foi, M. Trimeche, V. Katkovnik, and K. Egiazarian, "Practical Poissonian-Gaussian noise modeling and fitting for single-image raw-data," *IEEE Transactions on Image Processing*, vol. 17, no. 10, pp. 1737–1754, 2008.
- [6] F. Luisier, T. Blu, and M. Unser, "Image denoising in mixed Poisson-Gaussian noise," *IEEE Transactions on Image Processing*, vol. 20, no. 3, pp. 696–708, 2011.
- [7] M. Aharon, M. Elad, and A. Bruckstein, "K-SVD: An algorithm for designing overcomplete dictionaries for sparse representation," *IEEE Transactions on Signal Processing*, vol. 54, no. 11, pp. 4311–4322, 2006.
- [8] S. Gu, L. Zhang, W. Zuo, and X. Feng, "Weighted nuclear norm minimization with application to image denoising," in *Computer Vision and Pattern Recognition (CVPR)*, 2014.
- [9] K. Dabov, A. Foi, V. Katkovnik, and K. Egiazarian, "Image denoising by sparse 3-D transform-domain collaborative filtering," *IEEE Transactions on Image Processing*, vol. 16, no. 8, pp. 2080–2095, 2007.
- [10] D. Zoran and Y. Weiss, "From learning models of natural image patches to whole image restoration," in *International Conference on Computer Vision (ICCV)*, 2011.
- [11] T. Huang, S. Li, X. Jia, H. Lu, and J. Liu, "Neighbor2Neighbor: A self-supervised framework for deep image denoising," *IEEE Transactions on Image Processing*, 2022.
- [12] X. Ma, X. Lin, M. El Helou, and S. Süsstrunk, "Deep Gaussian denoiser epistemic uncertainty and decoupled dual-attention fusion," in *IEEE International Conference on Image Processing (ICIP)*, 2021, pp. 1–4.
- [13] K. Zhang, W. Zuo, and L. Zhang, "FFDNet: Toward a fast and flexible solution for CNN-based image denoising," *IEEE Transactions on Image Processing*, vol. 27, no. 9, pp. 4608–4622, 2018.
- [14] M. El Helou and S. Süsstrunk, "BIGPrior: Towards decoupling learned prior hallucination and data fidelity in image restoration," *IEEE Transactions on Image Processing*, 2022.
- [15] M. El Helou, R. Zhou, and S. Süsstrunk, "Stochastic frequency masking to improve super-resolution and denoising networks," in *European Conference on Computer Vision (ECCV)*, 2020, pp. 749–766.
- [16] A. Jezierska, H. Talbot, C. Chaux, J.-C. Pesquet, and G. Engler, "Poisson-gaussian noise parameter estimation in fluorescence microscopy imaging," in *2012 9th IEEE International Symposium on Biomedical Imaging (ISBI)*, 2012, pp. 1663–1666.
- [17] B. Zhang, "Contributions to fluorescence microscopy in biological imaging: PSF modeling, image restoration, and super-resolution detection," Thesis, Télécom ParisTech, Nov. 2007. [Online]. Available: <https://pastel.archives-ouvertes.fr/pastel-00003273>
- [18] D. Martin, C. Fowlkes, D. Tal, and J. Malik, "A database of human segmented natural images and its application to evaluating segmentation algorithms and measuring ecological statistics," in *Proc. 8th Int'l Conf. Computer Vision*, vol. 2, July 2001, pp. 416–423.